RSC Advances

PAPER

View Article Online
View Journal | View Issue

Check for updates

Cite this: *RSC Adv.*, 2026, **16**, 26778

Microreactor-assisted synthesis of surface-active oxygen-rich Mn–Ce oxide particles and their catalytic activity in the wet air oxidation process

Tenta Yamaryo, Takumi Hatashita and Noritsugu Kometani *

Received 6th February 2026
Accepted 29th April 2026

DOI: 10.1039/d6ra01056c

rsc.li/rsc-advances

In this study, a central-collision type microreactor was applied to the synthesis of Mn–Ce oxide catalysts by a liquid-phase oxidation method, which suffers from poor homogeneity and therefore has not been widely used in catalyst synthesis. This approach aimed to achieve improved structural homogeneity and oxygen defect formation. As a model reaction, phenol degradation by catalytic wet air oxidation was investigated using synthesized δ-type Mn–Ce oxides as catalysts. Compared with conventional stirring synthesis, microreactor-assisted synthesis afforded catalysts with finer and more uniform particles, larger specific surface areas, higher concentrations of surface oxygen species and bulk oxygen defects, and highly dispersed CeO_2 within the MnO_2 matrix. When applied to phenol degradation, a degradation efficiency of 57% after a reaction time of 1 h was achieved for the catalyst synthesized using the microreactor, in contrast to 43% for the catalyst synthesized by conventional stirring. These findings demonstrate that microreactor-assisted synthesis effectively incorporates unstable oxygen species into the catalyst structure, resulting in the enhancement of the efficiency of oxidative degradation reactions.

1. Introduction

The development of high-performance oxide catalysts plays a crucial role in diverse fields, including environmental preservation, energy conversion, and the removal of hazardous substances. In particular, catalytic reactions mediated by oxygen vacancies not only facilitate highly efficient redox processes but also exhibit remarkable selectivity, leading to widespread industrial applications.[1–6] Unlike conventional catalytic reactions that proceed *via* the Langmuir–Hinshelwood or Eley–Rideal mechanisms, these reactions are generally considered to follow the Mars–van Krevelen (MvK) mechanism. In this mechanism, the oxygen storage capacity of the catalyst, the amount of surface oxygen species serving as active sites, and the valence changes of the constituent elements involved in the reaction are key factors governing catalytic performance.[1,3,7–9]

Representative synthetic methods for oxide catalysts include co-precipitation, sol–gel processing, hydrothermal synthesis, and solvothermal methods. However, all of these methods require high-temperature treatments, which lead to particle coarsening and stabilization of lattice oxygen, ultimately resulting in a decreased oxygen storage capacity.[10–13] In contrast, liquid-phase oxidation, in which metal precursors are oxidized by oxidizing agents, is a rare approach that enables the formation of oxides under ambient conditions. However, unlike conventional methods, this approach suffers from the difficulty in producing fine and uniform particles. In general, particle size reduction and uniformity are achieved through nucleation and growth governed by the LaMer model or the Watzky–Finke mechanism. The LaMer model suggests that uniform particle sizes arise from the temporal separation of rapid nucleation and subsequent growth.[14] In contrast, the Watzky–Finke mechanism describes particle size control through slow, continuous nucleation coupled with autocatalytic growth.[15,16]

In liquid-phase oxidation, the metal species can undergo multiple valence transitions (*e.g.*, $M^{(n-2)+} \rightarrow M^{(n-1)+} \rightarrow M^{n+}$), resulting in a non-constant supply rate of Mn^{n+} monomers required for oxide precipitation. As a result, the temporal separation of nucleation and growth cannot be established, making size control by LaMer mechanism, as observed in liquid-phase reduction methods, difficult. Moreover, Ostwald ripening occurs during the growth stage under conditions of inhomogeneous M^{n+} monomer supply, hindering growth by Watzky–Finke mechanism typically observed in hydrothermal synthesis. Consequently, this process often results in particle coarsening and elemental segregation. Indeed, previous reports have demonstrated that oxides synthesized *via* liquid-phase oxidation are generally inhomogeneous and can grow into large particles exceeding several micrometers.[17,18]

To improve the aforementioned situations, this study propose a synthesis strategy for oxide catalysts *via* liquid-phase oxidation using a central-collision-type microreactor (K–M reactor). By reducing the channel dimensions to the microscale, microreactors provide four distinctive features: (1) rapid mixing

---

Department of Chemistry and Bioengineering, Graduate School of Engineering, Osaka Metropolitan University, 3-3-138 Sugimoto, Sumiyoshi-ku, Osaka 558-8585, Japan. E-mail: kometani@omu.ac.jp

through shortened diffusion distances, (2) precise fluid control within confined spaces, (3) efficient heat transfer enabling rapid heating and cooling, (4) accurate control of residence times on the millisecond scale. Exploiting these characteristics, microreactors have been successfully applied to the synthesis of finer nanoparticles compared to conventional simple stirring-mixing synthesis,[19–23] alloy nanoparticles composed of elemental combinations otherwise difficult to form solid-solution,[24,25] and oxide nanoparticles enriched with oxygen vacancies.[26,27]

Among the various types of microreactors, the K–M reactor is specifically designed to maximize these advantages and achieve instantaneous and homogeneous mixing. The K–M reactor introduces two or more fluid streams through microchannels in opposing or orthogonal directions, forcing them to collide at the center. This collision generates intense local shear forces and turbulence, enabling highly efficient and uniform mixing within an extremely short time.[28] In conventional micromixers, mixing relies predominantly on molecular diffusion, requiring extended time and distance to achieve sufficient homogeneity. In contrast, the K–M reactor introduces forced mixing through physical collision energy, thereby providing excellent performance even for highly viscous fluids or in synthetic processes demanding rapid reactions.[29,30] The forced, instantaneous, and homogeneous mixing achieved by the K–M reactor is expected to provide the following advantages during catalyst synthesis:

- Uniform reaction rates through enhanced molecular diffusion.
- Increased concentration of oxygen vacancies within the crystal lattice.
- Improved dispersion of heterogeneous metals.
- Uniform particle size distribution.
- Particle size refinement *via* accelerated nucleation kinetics.

By utilizing these properties, the application of the K–M reactor to liquid-phase oxidation enables the design of catalysts with enhanced performance and greater reproducibility.

Manganese–cerium mixed oxide catalysts, composed of inexpensive raw materials, are well recognized for their high catalytic activity in advanced oxidation processes (AOPs), including catalytic wet air oxidation (CWAO).[31] Among manganese oxides, the birnessite-type structure (δ-MnO_2) has been reported to be excellent at activating oxygen *via* oxygen vacancies compared with other crystal phases. Moreover, its layered structure provides high tolerance against structural distortion during redox cycling and offers abundant active sites.[32–35] In phenol degradation, redox reactions involving surface-active oxygen species in manganese oxides proceed spontaneously even in the absence of oxygen.[36] Meanwhile, under an oxygen atmosphere, phenol is oxidized by surface-active oxygen species in the catalyst ($Mn^{4+} \rightarrow Mn^{3+}$), followed by re-oxidation of Mn^{3+} to Mn^{4+} by dissolved oxygen in the aqueous phase. This cyclic process drives the reaction according to the MvK mechanism.[32] In addition, cerium doping has been shown to regulate the manganese oxidation state by promoting the formation of catalytically active Mn^{3+} species while suppressing the generation of less reactive Mn^{2+} species.[32] Cerium doping also stabilizes the preferential exposure of the (100) facet during crystal growth, which facilitates oxygen activation and enhances both oxygen supply capacity and surface reactivity of the catalyst.[32,33] However, the formation of such structures during synthesis requires the oxidation of Mn^{2+}, a process in which manganese may exist in multiple valence states (Mn^{7+}, Mn^{4+}, Mn^{3+}, Mn^{2+}). Differences in their redox kinetics often result in particle overgrowth and broad particle-size distributions.[18,32] Furthermore, CeO_2 exhibits limited solid solubility with manganese oxides and tends to aggregate or segregate, thereby reducing the overall homogeneity of the catalyst.[31]

To overcome these challenges, the K–M reactor, which enables instantaneous and homogeneous mixing, was employed, thereby allowing the immediate supply of Mn^{4+} and inducing nucleation and growth by the LaMer mechanism. Using this approach, we aimed to reproducibly synthesize nanosized Mn–Ce oxide particles. The catalytic activity of the oxides prepared using the K–M reactor was then compared with that obtained by the conventional stirring-mixing method, in order to assess the effectiveness of microreactor-assisted catalyst synthesis.

2. Experimental

2.1 Synthesis of Mn–Ce oxide

Catalysts were synthesized by a conventional redox-precipitation method.[37] The main reactions are represented as follows:

$$MnO_4^- + 3e^- + 2H_2O \rightarrow MnO_2 + 4OH^-$$

$$Mn^{2+} + 4OH^- \rightarrow MnO_2 + 2e^- + 2H_2O$$

$$Ce^{3+} + 4OH^- \rightarrow CeO_2 + e^- + 2H_2O$$

For a target Mn : Ce molar ratio of 9 : 1, a 0.54 mM aqueous solution of $KMnO_4$ (adjusted to pH 8 with KOH) and a 2.5 mM aqueous solution containing $Mn(NO_3)_2 \cdot 6H_2O$ and $Ce(NO_3)_3 \cdot 6H_2O$ were prepared. Note that the Mn : Ce molar ratio of 9 : 1 was chosen, because this ratio exhibited the highest catalytic activity in previous studies.[32] As depicted in Fig. 1, these solutions were introduced into the K–M reactor at flow rates of 20 mL min^{-1} and 10 mL min^{-1}, respectively, using Pu-2080 HPLC pumps (JASCO, Japan) at 60 °C to obtain the Mn–Ce oxide catalysts. Note that it has been confirmed that the outer surface temperature of the K–M reactor remained almost constant at 60 °C during the reaction. The schematic structure of the K–M reactor used in this study is illustrated in Fig. 2. The body of the mixer is made of stainless steel and it was designed for two types of solutions to pass through seven microchannels (200 μm in diameter) and collide each other in the center (350 μm in diameter), allowing for the forced, instantaneous, and homogeneous mixing. The resulting precipitates were collected by vacuum filtration and dried overnight at 60 °C.

For comparison, reference catalysts were synthesized under identical conditions without the K–M reactor by directly mixing the solutions in a vessel with stirring for 30 min, and subsequently recovered by vacuum filtration and dried overnight at

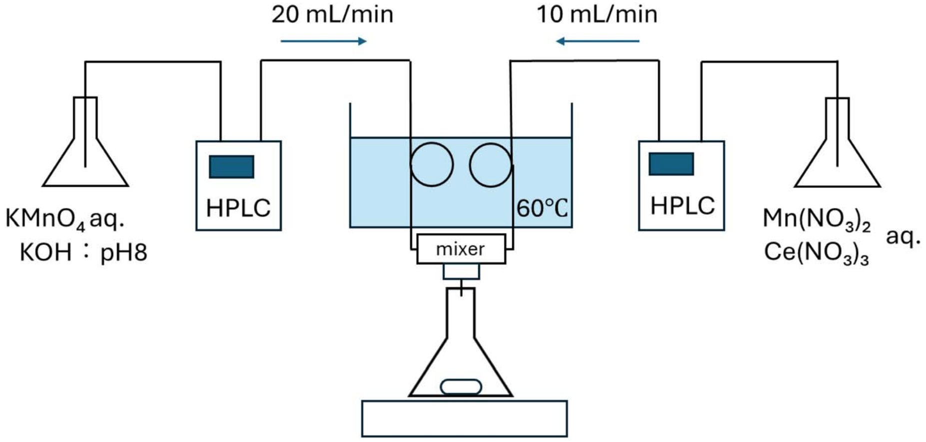

Fig. 1 Schematic illustration of the experimental apparatus used for the synthesis of Mn–Ce oxide catalyst with the K–M reactor.

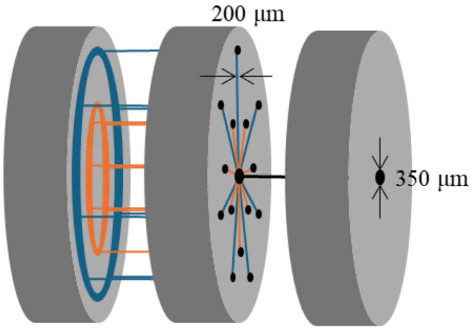

Fig. 2 Schematic illustration of the K–M reactor used in this study. The two types of solutions, shown in blue and orange, pass through seven microchannels (200 μm in diameter) and collide in the center (350 μm in diameter).

60 °C (this procedure is hereafter referred to as "the stirring-mixing method").

2.2 Characterization

Elemental analysis by X-ray fluorescence (XRF) was performed using a JSX-1000S spectrometer (JEOL, Japan) equipped with a Rh target. The measurements were carried out under conditions of 50 kV tube voltage and 1 mA tube current, using the built-in silicon drift detector. UV-visible absorption spectroscopy was conducted on a UV-3600 spectrophotometer (Shimadzu, Japan). Sample solutions were loaded into quartz cells with optical path length of 1 cm. X-ray diffraction (XRD) patterns of catalysts were obtained using a MiniFlex600-C diffractometer (Rigaku, Japan) with the θ–2θ scanning mode. Data were collected over a 2θ range of 3–90° with a step size of 0.01° and a scanning rate of 2° min^{-1}. Powder samples were analyzed without any special pretreatment. Transmission electron microscopy (TEM) was carried out on a JEM-2100plus microscope (JEOL, Japan) operated at an accelerating voltage of 200 kV. TEM specimens were prepared by ultrasonically dispersing 0.01 g of sample in 10 mL of toluene, followed by drop-casting and drying onto the carbon-coated Cu grid. Particle size analysis was performed using ImageJ software. The analysis by STEM-EDS (bright-field) was conducted using a large solid-angle EDS detector (100 mm^2).

Nitrogen adsorption–desorption isotherms were measured on a BELSORP MINI X instrument (MicrotracBEL, Japan). Prior to analysis, samples were degassed overnight at 120 °C under vacuum using a BELPREP VAC III system (MicrotracBEL, Japan). Adsorption measurements were performed by the volumetric method with nitrogen as the adsorbate at 77 K (liquid nitrogen temperature). The specific surface area was calculated by the BET method in the relative pressure range of 0.1–0.25. The adsorption isotherm analysis was performed following a previously reported procedure.[38]

XPS spectra were acquired on an ESCA-3400 spectrometer (Shimadzu, Japan). Samples were mounted on conductive carbon tape and held under vacuum for 10 min prior to analysis. Al Kα radiation was used as the X-ray source, and the binding energies were calibrated against the C 1s peak at 284.5 eV. Data analysis was carried out using the built-in software of the ESCA-3400, and Shirley-type background subtraction was applied. The background correction range was adjusted so that the integrated area ratios of Mn $2p_{1/2}$ to $2p_{3/2}$ and Ce $3d_{3/2}$ to $3d_{5/2}$ approximately matched 1 : 2 and 2 : 3, respectively. When fitting the Mn 2p spectra, the energy separation between $2p_{1/2}$ and $2p_{3/2}$ was fixed at 11.7 eV, and the peak area ratio was set to 1 : 2. The Mn 3s spectra were analyzed without constraints, and only the peak-top positions were determined. For fitting the Ce 3d, the energy separation between $3d_{3/2}$ and $3d_{5/2}$ was fixed at 18.10 eV, and the peak area ratio was adjusted to 2 : 3.

Raman spectra were recorded using an NRS-4500 spectrometer (JASCO, Japan) in micro-Raman mode. Samples were mounted on glass slides. The measurement conditions were as follows: excitation wavelength, 532.08 nm; laser power, 6.2 mW; spectral resolution, 1 cm^{-1}; accumulation, three scans. Exposure time was adjusted depending on the sample. No special pretreatment was applied prior to measurement.

H_2-temperature programmed reduction (H_2-TPR) experiments were carried out on a BELCAT II-SPTT instrument equipped with a thermal conductivity detector (MicrotracBEL, Japan). Prior to analysis, 0.05 g of sample was pretreated in an Ar flow (30 mL min^{-1}) at 200 °C for 2 h. Subsequently, 5% H_2/Ar (30 mL min^{-1}) was introduced, and the sample was heated to 900 °C at a ramping rate of 10 °C min^{-1}. The H_2 consumption was quantitatively determined from a calibration curve constructed using the pulse method.

2.3 Catalytic test for phenol degradation experiments

Phenol degradation experiments by CWAO were carried out using a titanium-made batch reactor (internal volume 50 cm^3) sealed with graphite gaskets. 0.01 g of catalyst and 25 cm^3 of an aqueous phenol solution (100 ppm) were sealed in the reactor and then O_2 gas was injected at 2 MPa. The reactor was heated at 150 °C with an electric furnace and reacted for 0.5–2 hours (above 200 °C, a distinct colour change of the catalyst was observed, clearly indicating catalyst deactivation. In contrast, as the temperature decreased, the difference from the reaction conducted under a nitrogen atmosphere became negligible, suggesting that the process was no longer dominated by catalytic reactions. Based on these observations, the reaction temperature was set to 150 °C). After the reaction, the reactor was quenched in a water bath and the phenol and TOC concentrations were determined using a liquid chromatography (LC) equipped with an UV detector (Prominence series, Shimadzu) and a TOC analyzer (TOC-V CSN, Shimadzu), respectively. For LC, a Kinetex C18 column (2.6 μm, 100 Å, 150 × 4.6 mm I.D.) was employed and the mobile phase consisted of a mixture of acetonitrile (200 mL), distilled water (200 mL), and phosphoric acid (400 μL). Measurements were performed at a flow rate of 0.5 cm^3 min^{-1} with the column oven maintained at 40 °C and the detection wavelength set at 214 nm. The phenol decomposition ratio and TOC removal ratio were calculated using the following equations:

$$\text{Decomposition ratio} = 1 - (\text{phenol concentration after reaction}/\text{phenol concentration before reaction})$$

$$\text{TOC removal ratio} = 1 - (\text{TOC concentration after reaction}/\text{TOC concentration before reaction})$$

Phenol degradation experiments under N_2 atmosphere were conducted by repeatedly purging with N_2 to completely remove O_2, followed by sealing with N_2 at 2 MPa. All other experimental conditions, including temperature, catalyst amount, and solution volume, were identical to those used under O_2 atmosphere. To ensure reproducibility, each experiment was conducted three times, and the average values were reported. After the reaction, the catalyst recovered by vacuum filtration was dried at room temperature under reduced pressure and then used for characterization.

3. Results and discussion

The elemental ratios of the catalysts determined by XRF analysis are summarized in Table 1. The elemental ratio of Mn : Ce in the catalysts synthesized by the stirring-mixing method and those synthesized using the K–M reactor was roughly the same at 7 : 3. However, this value deviated from the molar ratio of the starting precursors (Mn : Ce = 9 : 1). This discrepancy can be attributed to the incomplete consumption of Mn^{7+}, which remained in the filtrate after the reaction, as confirmed by the UV-Vis absorption spectra shown in Fig. S1. Furthermore, the pH of the filtrate after the reaction decreased to 3.45. As the redox reaction progresses, protons (H^+) are produced, causing the pH to gradually decrease as the reaction progresses. Notably, in the redox reaction between Mn^{7+} and Mn^{2+}, the overall redox potential becomes negative when the pH falls below 3.75, rendering the Gibbs free energy change (ΔG) positive. Under such conditions, the reaction will reach a thermodynamically unfavourable state and will stop before completing, leaving both Mn^{7+} and Mn^{2+} in the solution. Consequently, the Mn content in the final catalyst was lower than the precursor molar ratio. In contrast, for the redox reaction between Ce^{3+} and Mn^{7+}, the critical pH at which ΔG becomes zero is 1.06. In this experiment, the pH of the solution after reaction was 3.45. Thus, ΔG remained significantly negative, indicating that Ce^{3+} has reacted almost completely. As a result, it is presumed that both Mn^{7+} and Mn^{2+} remained partially unreacted in the reaction system, and the Mn content in the product was lower than the precursor concentration ratio.

Table 1 Elemental compositions of the Mn–Ce oxides synthesized by the conventional stirring-mixing method and those synthesized using the K–M reactor, determined by XRF (unit: %)

Elements	Stirring	K–M reactor
K	0.16	0.27
Mn	71.09	71.15
Cu	0.07	0.07
Ce	28.67	28.52

Next, the crystal structures of the synthesized catalysts were examined by XRD (Fig. 3). In all samples, diffraction peaks corresponding to the (100) and (110) planes of δ-MnO_2 were observed at around 2θ = 37° and 66°, respectively (JCPDS No. 80-1098). In contrast, the catalyst synthesized from only Mn

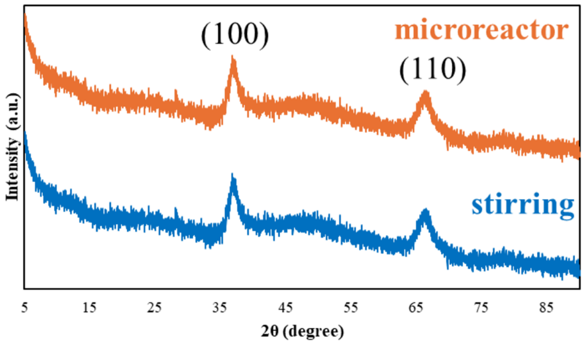

Fig. 3 XRD patterns of the catalysts synthesized with a nominal Mn : Ce molar ratio of 9 : 1.

exhibited additional peaks assigned to other crystal planes such as the (001) plane (Fig. S2). Previous studies have reported that oxygen vacancies located on the (100) plane are more favourable for O_2 activation than those formed on the (001) plane.[33] Therefore, the enhanced exposure of the (100) plane induced by Ce incorporation in this study is likely to facilitate the generation of reactive oxygen species within the catalyst, thereby contributing to the improved catalytic activity.

Furthermore, in the Ce-rich catalyst with a nominal Mn : Ce ratio of 5 : 1 (XRF ratio = 6 : 4), additional diffraction peaks attributed to CeO_2 were detected only in the catalyst synthesized by the stirring-mixing method (Fig. S2). This indicates that, under conventional stirring conditions, Ce tends to locally aggregate, leading to phase separation as CeO_2. In contrast, no CeO_2-related peaks were detected in the catalyst synthesized using the K–M mixer. These results suggest that the instantaneous and forced mixing in the K–M reactor promotes more uniform nucleation and enables highly dispersed incorporation of Ce into the MnO_2 crystal lattice.

To evaluate the particle size and surface characteristics of the catalysts, TEM observations and nitrogen adsorption–desorption measurements were performed. As shown in Fig. 4a, TEM observations revealed that catalysts obtained by the stirring-mixing method predominantly consisted of large particles exceeding 1 μm with irregular morphologies, making it difficult to establish a clear particle size distribution. In contrast, catalysts synthesized using the K–M reactor exhibited uniform, spherical particles with an average size of approximately 300 nm (Fig. 4b and c). These findings demonstrate that the microreactor-assisted synthesis makes it possible to obtain finer particles with a much narrower size distribution. Based on these results, it is suggested that the instantaneous and forced mixing within the K–M reactor facilitated a more homogeneous redox reaction, leading to the rapid supply of Mn^{4+} monomers. Consequently, it is presumed that the immediate nucleation of MnO_2 and subsequent crystal growth under a uniform environment were induced, resulting in the formation of finer particles with a narrower size distribution in accordance with the LaMer mechanism.

Nitrogen adsorption–desorption measurements revealed type IV isotherms with H3-type hysteresis loops for both samples (Fig. S3), indirectly indicating the presence of layered structures. Moreover, the catalyst synthesized using the K–M reactor exhibited a higher specific surface area (100.1 $m^2 g^{-1}$) than that prepared by the stirring-mixing method (91 $m^2 g^{-1}$) (Fig. S4). In layered structures, the specific surface area is expected to increase as the number of stacked layers decreases and the lateral dimension of each layer becomes larger. Previous studies have further demonstrated that an enhanced supply rate of Mn^{4+} ions contributes to the enlargement of the surface area per layer.[18] It is thus suggested that the K–M reactor promoted a more uniform reaction environment and accelerated the supply of Mn^{4+} monomers, thereby enlarging the surface area per layer and ultimately leading to an increased overall surface area.

Next, the chemical states of the elements present on the catalyst surface were investigated by XPS. The XPS wide spectra are shown in Fig. S5, demonstrating the presence of Mn, Ce and

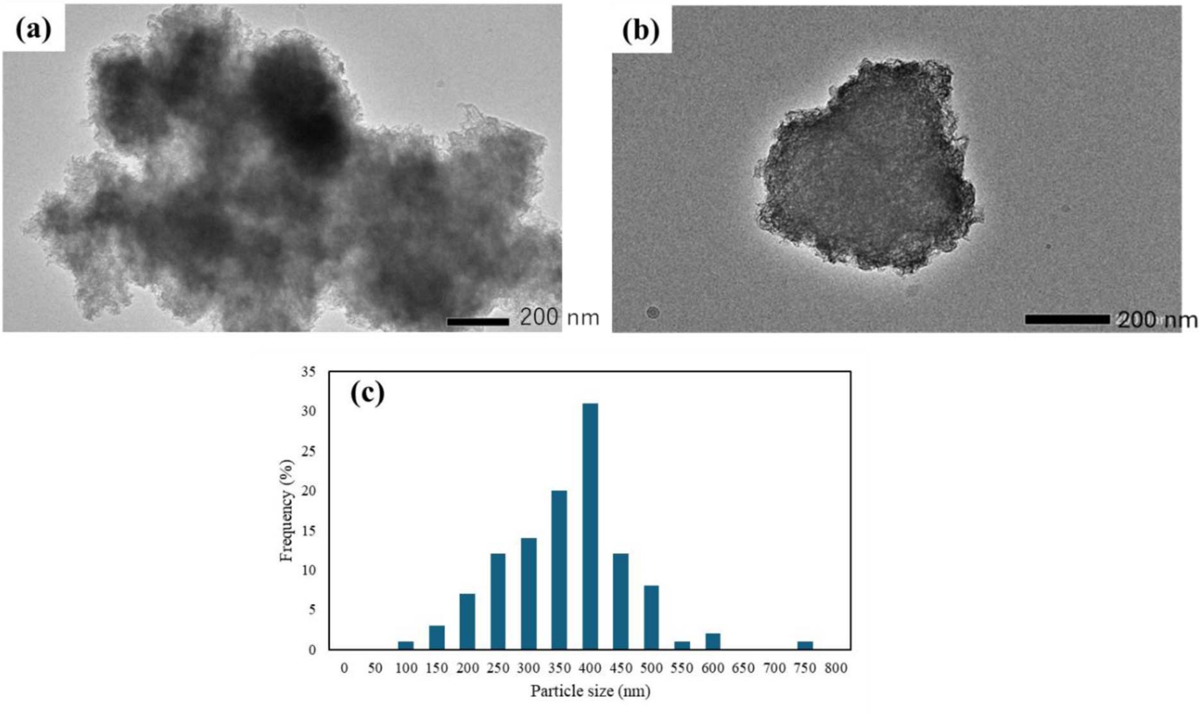

Fig. 4 (a) TEM image of Mn–Ce oxide particles obtained by stirring-mixing method. (b) TEM image and (c) size distribution of Mn–Ce oxide particles synthesized using the K–M reactor. The size distribution was estimated by analysing 112 particles randomly selected from the TEM images.

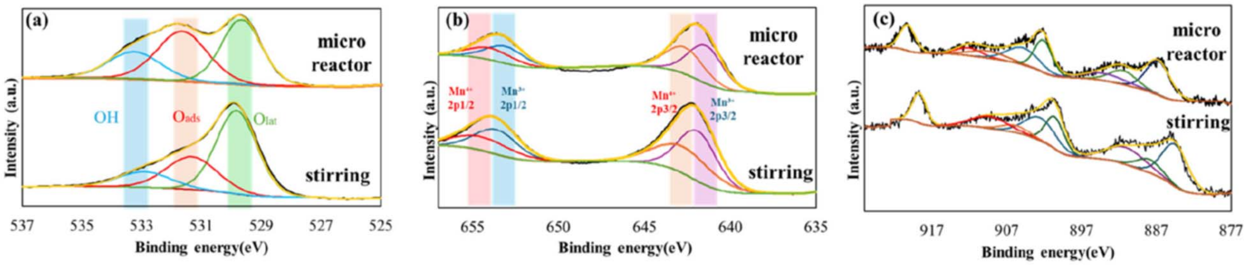

O 1s	OH (%)	O_{ads} (%)	O_{lat} (%)
stirring	13.86	28.41	57.73
microreactor	21.67	38.41	39.92

Mn 2p	Mn^{3+} (%)	Mn^{4+} (%)
stirring	55.52	44.49
microreactor	55.72	44.28

Fig. 5 (a) O 1s XPS spectra of the catalysts synthesized by each method and the corresponding peak area ratios (%). (b) Mn 2p XPS spectra of the catalysts synthesized by each method and the Mn^{4+}/Mn^{3+} area ratios (%) calculated from the sum of the $2p_{1/2}$ and $2p_{3/2}$ components. (c) Ce 3d XPS spectra of the catalysts synthesized by each method.

O in the prepared catalysts. In the O 1s spectrum (Fig. 5a), the peak at about 533.1 eV was assigned to hydroxyl groups (OH), the peak at about 531.5 eV was attributed to surface-active oxygen species such as O_2^{2-} and O^- (O_{ads}), and the peak at about 529.6 eV was assigned to lattice oxygen (O_{lat}).[39] Curve fitting of these peaks followed by quantitative comparison of their relative areas revealed that the peak corresponding to O_{ads} was significantly enhanced for the catalyst synthesized using the K–M reactor. This phenomenon can be rationalized by two factors. First, as confirmed by the N_2 adsorption–desorption analysis, the uniform and rapid mixing in the K–M reactor promoted particle refinement and increased the specific surface area, thereby leading to a greater abundance of O_{ads}. Second, instantaneous mixing resulted in the formation of oxygen vacancies, while strong oxidation at defect sites by residual potassium permanganate in solution further promoted the generation and accumulation of unstable O_{ads}.

In the Mn 2p spectrum (Fig. 5b), the peak at about 653.5 eV was assigned to Mn^{3+} in Mn $2p_{1/2}$, the peak at about 652.5 eV to Mn^{4+} in Mn $2p_{1/2}$, the peak at about 642 eV to Mn^{3+} in Mn $2p_{3/2}$, and the peak at about 641 eV to Mn^{4+} in Mn $2p_{3/2}$.[39] Since no satellite peak characteristic of Mn^{2+} was observed, its presence was excluded, and the peak assignments were made solely on the basis of Mn^{3+} and Mn^{4+}. Comparison of these peaks indicated that the Mn valence states on the catalyst surface were not affected by the synthesis method. This finding was consistent with the average oxidation states of Mn estimated from the Mn 3s peaks (Fig. S6).[40]

The chemical states of Ce was evaluated using the Ce 3d spectrum (Fig. 5c).[39,41] The Ce 3d spectrum consists of multiple overlapping peaks originating from Ce^{3+} and Ce^{4+}, making curve fitting and quantitative analysis of the relative peak areas difficult. Nevertheless, the peak located at about 920 eV is known to arise from a characteristic electronic transition of Ce^{4+}. In this study, this peak was clearly observed, confirming the presence of Ce^{4+} species in the catalyst.

Raman spectroscopy was conducted to investigate the structural features and defects of the catalysts. Three distinct peaks were observed at approximately 572, 630, and 503 cm^{-1} (Fig. 6), which are characteristic of δ-MnO_2. These peaks can be assigned as follows:[42] 630 cm^{-1} to Mn–O stretching vibration, 572 cm^{-1} to Mn–O–Mn bending vibration, 503 cm^{-1} to deformation mode of MnO_6 octahedra. The fitting results for each peak using the Lorentz function are also tabulated in Fig. 6. Comparison of the catalyst prepared by the stirring-mixing method with that synthesized using the K–M reactor revealed that only the later exhibited broadening and a slight red-shift of the Mn–O stretching vibration at 630 cm^{-1}. Such broadening and shifting of the stretching mode are typically associated with a decrease in the average oxidation state of Mn, *i.e.*, an increase

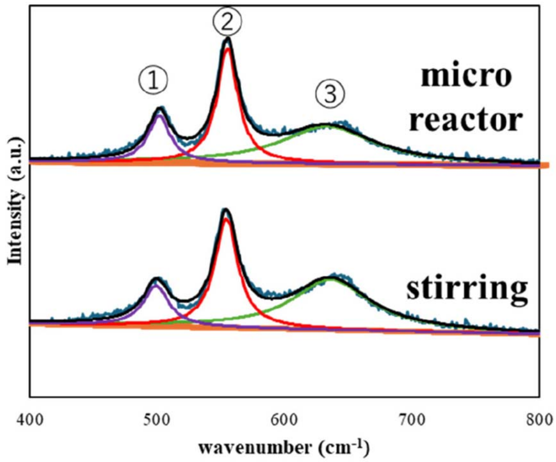

stirring	width (cm^{-1})	height	area (%)
①	21.1	107	15.0
②	19.9	263.4	34.8
③	88.1	86	50.2

stirring	width (cm^{-1})	height	area (%)
①	24.4	93.3	13.9
②	22.3	249.9	34.0
③	73.6	116.1	52.1

Fig. 6 Raman spectra of the catalysts synthesized by each method and the results of fitting each peak using the Lorentz function.

in Mn^{3+} species. The Jahn–Teller effect of Mn^{3+} introduces variations in the Mn–O bond length, leading to peak broadening and shifts in the Raman spectrum.[43] Accordingly, the catalyst synthesized using the K–M reactor contains a higher proportion of Mn^{3+}, which leads to the increased oxygen vacancies.

The discrepancy between the XPS and Raman results can be attributed to the different probing depths of the two techniques. XPS provides information from only a few nanometers below the surface, whereas Raman spectroscopy probes several micrometers into the bulk. At the catalyst surface, additional oxidation is promoted by residual $KMnO_4$ after synthesis, which accounts for the absence of valence differences in Mn as detected by XPS regardless of the synthesis method. In contrast, the bulk region is less affected by residual $KMnO_4$, so it strongly reflects the redox processes during nucleation and crystal growth. In the case of the K–M reactor, instantaneous molecular-level diffusion and forced mixing occur, rendering redox reactions rather than nucleation the rate-determining step. Consequently, Mn^{2+} is not fully oxidized to Mn^{4+} but is instead incorporated into the crystal lattice as Mn^{3+}. As a result, the catalyst synthesized by the K–M reactor exhibits a higher bulk fraction of Mn^{3+} compared to that synthesized by the stirring-mixing method.

The results of the H_2-TPR measurements are presented in Fig. 7. For the catalyst synthesized by the stirring-mixing method, three distinct reduction peaks were observed at 296 °C, 324.4 °C, and 426.4 °C. These peaks can be assigned to the reduction of $Mn^{4+} \rightarrow Mn^{3+}$ in Ce-free regions, $Mn^{4+} \rightarrow Mn^{3+}$ in the vicinity of Ce, and $Mn^{3+} \rightarrow Mn^{2+}$, respectively (Fig. 7a). The corresponding H_2 consumptions for these peaks were 1.228, 0.690, and 1.110 mmol g^{-1}, respectively. On the other hand, the catalyst synthesized using the K–M reactor exhibited two reduction peaks at 338.5 °C and 412.4 °C, which are attributable to the reduction of $Mn^{4+} \rightarrow Mn^{3+}$ near Ce and $Mn^{3+} \rightarrow Mn^{2+}$, respectively (Fig. 7b). The corresponding H_2 consumptions for these peaks were 4.457 and 1.226 mmol g^{-1}, respectively. In assigning these peaks, it was taken into account that the reduction of MnO_2 typically proceeds within the temperature range of 200–450 °C, generally giving rise to two peaks corresponding to $Mn^{4+} \rightarrow Mn^{3+}$ and $Mn^{3+} \rightarrow Mn^{2+}$ reductions.[44] Although it is well established that a decrease in particle size generally lowers the reduction temperature,[45] the peaks shifted to higher temperature for the catalyst synthesized using the K–M reactor in spite of smaller particle size. Previous studies have reported that Ce doping shifts the reduction peaks to higher temperature due to the strong Mn–Ce interactions,[45,46] and this effect appears to be particularly pronounced in the present work. Specifically, in the catalyst synthesized by the stirring-mixing method, the dispersion of CeO_2 was insufficient. Nevertheless, given that no aggregation was detected by STEM-EDS with a spatial resolution of several tens of nanometers, the degree of aggregation is presumed to be only on the order of a few nanometers (Fig. S7). As a consequence, distinct splitting of the reduction peaks was observed between regions in close proximity to CeO_2 and those away from Ce. In contrast, the catalyst synthesized using the K–M reactor has significantly improved dispersion of CeO_2, as evidenced by XRD results. It is conceivable that the substantial increase in the contact area between Mn and Ce led to the emergence of a single peak at higher temperature.

Furthermore, the H_2 consumption calculated from the $Mn^{4+} \rightarrow Mn^{3+}$ reduction peak in the catalyst synthesized using the K–M reactor was approximately twice that of the catalyst synthesized by the stirring-mixed method. This difference suggests that microreactor-assisted synthesis exerts a profound influence on both the abundance and spatial distribution of Mn species that serve as active sites. Indeed, as also implied by the results of Raman spectroscopy, the microreactor-assisted synthesis facilitates rapid nucleation, during which

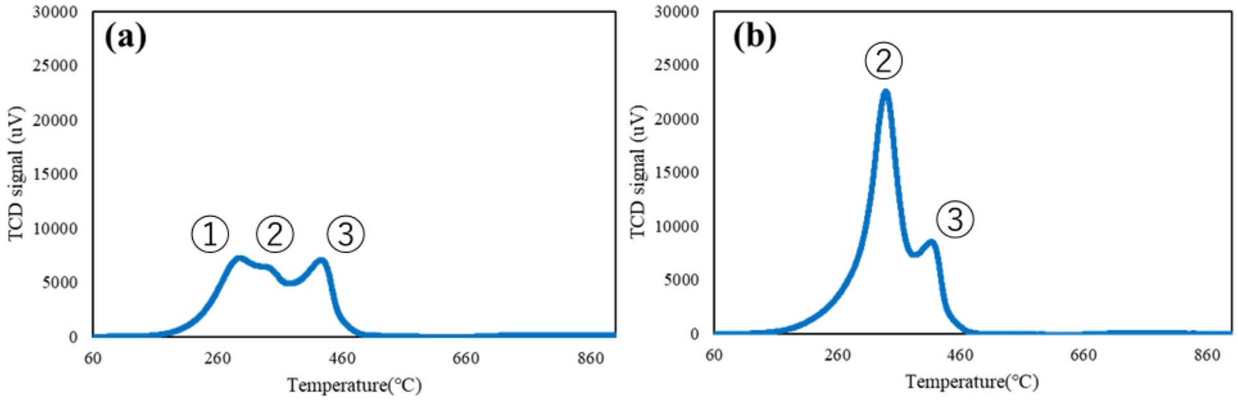

	peak temperature (°C)	H_2 consumption (mmol/g)
①	296	1.228
②	324.4	0.69
③	426.4	1.11

	peak temperature (°C)	H_2 consumption (mmol/g)
①	–	–
②	338.5	4.457
③	412.4	1.226

Fig. 7 H_2-TPR profiles along with the reduction peak temperatures and corresponding H_2 consumption values of (a) the catalyst synthesized by the stirring-mixing method, and (b) the catalyst synthesized using the K–M reactor.

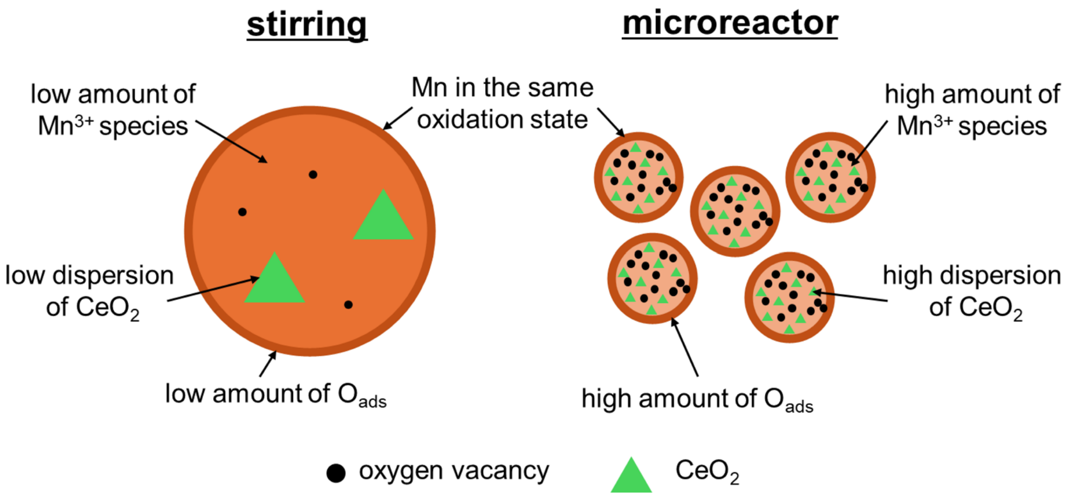

Fig. 8 Schematic illustration of Mn–Ce oxide catalysts synthesized by the stirring-mixing method and those synthesized using the K–M reactor, summarizing the characterization results and their interpretations.

a considerable amount of oxygen in an electronically unstable state is incorporated into the lattice. Under elevated temperatures, such oxygen is expected to migrate dynamically within the MnO_2 framework which possesses high oxygen mobility. Thus, the increased H_2 consumption observed for the catalyst synthesized using the K–M reactor can be rationalized by its higher content of unstable lattice oxygen compared with that synthesized by the stirring-mixed method.

Based on the above characterization results, the structures of catalyst particles synthesized by the conventional stirring-mixing method and those synthesized using the K–M reactor are illustrated in Fig. 8 and the following inferences were made regarding the generation mechanisms of oxygen vacancies and surface oxygen species (O_{ads}) in each synthesis method. First, compared to K–M reactor synthesis, the conventional stirring-mixing method results in a larger reaction field, leading to coarser catalyst particles and a tendency for decreased dispersibility of CeO_2 (green triangles in the figure) within the catalyst. Furthermore, the redox reaction proceeds heterogeneously in the conventional stirring-mixing, resulting in spatially heterogeneous Mn^{4+} concentrations. Consequently, the rate-determining step shifts from the redox reaction process to the nucleation process. This reaction environment is thought to have led to a decrease in the proportion of Mn^{3+} species, resulting in a reduction of oxygen vacancies (black circles in the figure).

On the other hand, synthesis using the K–M reactor resulted in accelerated molecular diffusion in a reaction field confined to a micrometer scale. This led to refinement of catalyst particles and improved dispersibility of CeO_2. Furthermore, it is thought that the redox reaction proceeds spatially uniformly, resulting in the homogeneous generation of Mn^{4+} species. As a result, the rate-determining step of the reaction becomes the redox process rather than the nucleation process, which is thought to promote an increase in oxygen vacancies and an increase in the proportion of Mn^{3+} species within the catalyst. This is consistent with the observations of the Raman spectra (low wavenumber shift, increase in full width at half maximum and decrease in peak area of the band attributed to the Mn–O stretching vibration appearing at 630 cm^{-1}). In addition, the oxygen vacancies on the catalyst surface are further oxidized by the remaining $KMnO_4$ and converted into the O_{ads}. Therefore, catalysts synthesized using a K–M reactor with a high oxygen vacancy concentration are thought to have more O_{ads} compared to catalysts synthesized by the conventional stirring-mixing method. This is also consistent with the observations of the XPS spectrum as shown in Fig. 5.

According to the previous study,[26] an increase in oxygen vacancies has also been reported for $Ce_{0.9}Y_{0.1}O_2$ and $Ni–Al_2O_3$ synthesized using a microreactor, suggesting that the microreactor synthesis strategy can be universally applied to other mixed oxides.

The mineralization of phenol over Mn oxide catalysts is known to proceed through the MvK mechanism, as illustrated in Fig. 9.[32] In this reaction mechanism, first, the O_{ads} exposed on the catalyst surface promote the oxidation reaction of phenol. Next, the oxygen vacancies created on the catalyst surface are re-oxidized by dissolved oxygen in the reaction solution, regenerating the O_{ads}. This cycle continues, and the catalytic reaction proceeds.

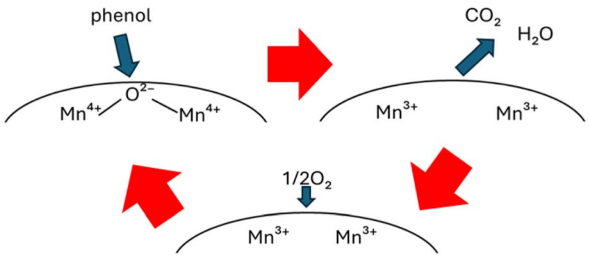

Fig. 9 Schematic illustration of phenol mineralization over Mn oxide catalysts based on the Mars–van Krevelen (MvK) mechanism.

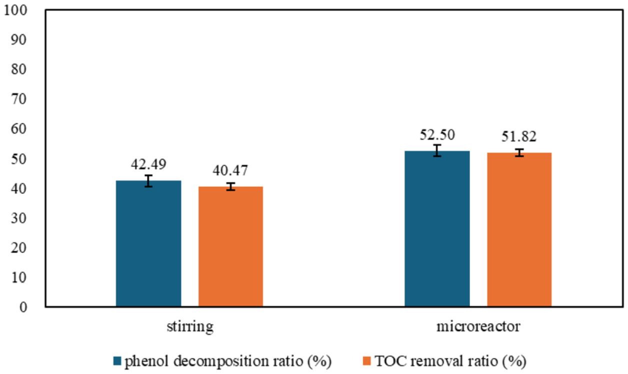

Fig. 10 Phenol decomposition ratio (%) and TOC removal ratio (%) at reaction time of 2 h by CWAO under nitrogen atmosphere using different catalysts.

Using the synthesized Mn–Ce oxides as catalysts, phenol degradation experiments by CWAO was first conducted under a nitrogen atmosphere to evaluate the amount of surface-active oxygen species consumed through a so-called sacrificial reaction which eliminated the reoxidation of the catalyst by oxygen. Under N_2, both phenol conversion and TOC removal ratio showed no significant difference between reaction times of 1 h and 2 h, indicating that the sacrificial reaction had completely ceased by 2 h. Therefore, the following discussion has been made based on the results obtained at 2 h. As shown in Fig. 10, the catalyst synthesized using the K–M reactor exhibited approximately 1.25 times higher phenol conversion and TOC removal ratio than that prepared by the stirred-mixing method. This enhancement can be attributed to an increase in the amount of active oxygen species on the catalyst surface for the microreactor-assisted synthesis. This interpretation is consistent with the XPS results, which showed that the fraction of O_{ads} increased by about 1.35 times, strongly supporting this conclusion. Furthermore, the Mn 2p XPS spectra obtained after the reaction under an N_2 atmosphere (Fig. S8) revealed that the catalyst synthesized using the K–M reactor exhibited a higher fraction of Mn^{3+} compared with that prepared by the stirring-mixing method. This result, consistent with the Raman spectroscopic analysis, suggests that a Mn^{3+}-rich structure is more stable within the catalyst synthesized using the K–M reactor than within that prepared by the conventional method. Moreover, this finding indirectly indicates that, for the microreactor-synthesized catalyst, the reduction of Mn^{4+} to Mn^{3+} on the catalyst surface proceeds more readily during the reaction, accompanied by an increased consumption of active oxygen species.

Next, the phenol degradation by CWAO under an oxygen atmosphere was investigated (Fig. 11). For both catalysts, phenol decomposition ratios and TOC removal ratios were almost the same at all reaction times, suggesting that no reaction intermediate was formed and phenol was completely mineralized once degradation began. Therefore, it was difficult to detect intermediate products supporting the MvK mechanism. This consideration was also supported by the fact that no change in pH was observed before and after the degradation reaction. It is noteworthy that the catalyst synthesized using the K–M reactor exhibited a phenol decomposition ratio approximately 15% higher than that of the catalyst prepared by conventional stirring-mixing method, at reaction time of 1 h. This result is consistent with the analysis of the O 1s spectrum by XPS, H_2-TPR measurements, and the phenol degradation experiments under N_2-atmosphere conditions, all of which revealed that the Mn–Ce oxide catalyst synthesized using the K–M reactor contains a larger amount of unstable oxygen species that contribute to the reaction. Therefore, it can be concluded that the microreactor-assisted synthesis introduces a higher concentration of surface-active oxygen species, leading to enhanced oxidation efficiency in phenol degradation.

On the other hand, after one hour of reaction, the difference in decomposition ratio remained almost constant at about 15%. This phenomenon is attributed to the fact that the concentration of dissolved oxygen in the aqueous phase is significantly lower than the concentration of catalyst. In fact, while the amount of catalyst added was 115 μmol (0.01 g), the dissolved oxygen concentration in water, calculated based on Henry's law, was limited to 7.75 μmol. XRD measurements after 2 h of reaction showed a decrease in crystallinity, and the Raman spectrum recorded after 2 h of reaction exhibited a significant

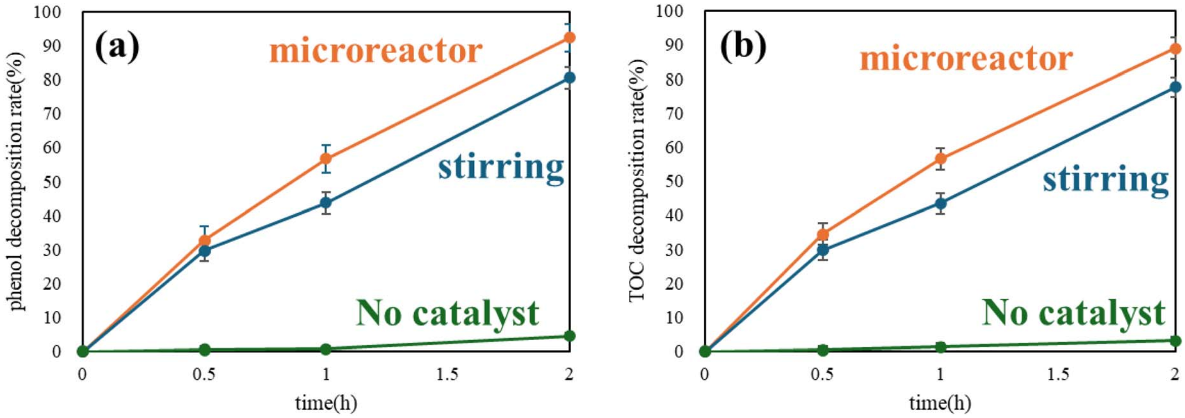

Fig. 11 Temporal changes in (a) phenol decomposition ratio and (b) TOC removal ratio by CWAO under an oxygen atmosphere using different catalysts or no catalyst.

shift toward lower wavenumbers (Fig. S9 and S10). This observation suggests that the proportion of Mn^{3+} increased during the reduction process, inducing lattice distortion *via* the Jahn–Teller effect. In addition, the Mn 2p XPS spectrum obtained after 2 h of reaction under an oxygen atmosphere (Fig. S11) revealed a decrease in the proportion of Mn^{4+} accompanied by an increase in the proportion of Mn^{3+}. Comparison with the Mn 2p XPS spectrum recorded after 2 h of reaction under a nitrogen atmosphere showed that, although the fraction of Mn^{3+} under oxygen was slightly lower than that under nitrogen, the overall spectral features were nearly identical. In other words, as the reaction proceeded, the surface-active oxygen species on the catalyst was fully consumed, making the re-oxidation of the catalyst by the dissolved oxygen the rate-determining step. As a result, the difference in decomposition ratio gradually became constant. For reference, the results of the experiments conducted under different O_2 pressure conditions are shown in Fig. S12. It can be seen that, for both synthesis methods, the phenol decomposition ratios and the TOC removal ratios increase in the order of 2 MPa N_2 < 1 MPa O_2 < 2 MPa O_2. These results further support that the re-oxidation of the catalyst by dissolved oxygen is the rate-determining step of the reaction.

Finally, the elemental analysis by XRF measurements was performed for each catalyst before and after 2 h of the degradation experiments (Table S1), which revealed that the catalyst synthesized using the K–M reactor exhibited little change in the elemental composition compared with that prepared by the conventional stirring-mixing method, suggesting reduced Mn leaching and improved stability during the reaction.

4. Conclusion

In this study, it was demonstrated that liquid-phase oxidation using a central-collision type microreactor provides significant advantages over conventional stirring-mixing methods for the synthesis of δ-type Mn–Ce oxides. The microreactor enabled the formation of finer and more homogeneous particles, high dispersion of CeO_2 within the MnO_2 matrix, and a greater density of surface oxygen species and lattice oxygen vacancies. Characterization by H_2-TPR and phenol degradation under N_2 confirmed that microreactor-assisted synthesis markedly increases the number of active sites involved in the redox cycle. When applied to catalytic wet air oxidation of phenol, the catalyst synthesized using the microreactor exhibited more excellent performance, achieving a decomposition ratio of 56.7 ± 5.7% after reaction time of 1 h, compared to 43.7 ± 2.8% for the conventional counterpart. This enhanced activity was attributed to the abundance of surface-active oxygen species that facilitate oxidation reactions.

Overall, these results establish microreactor-assisted synthesis as an effective and versatile strategy for designing oxygen-deficient mixed oxides with high catalytic activity, opening new avenues for advanced catalyst development in oxidative degradation processes and broader applications in environmental remediation and energy conversion.

Author contributions

Tenta yamaryo: data curation, formal analysis, investigation, methodology, writing– original draft, Takumi Hatashita: data curation, formal analysis, Noritsugu Kometani: project administration, supervision, validation, formal analysis, methodology, writing– review & editing, resources.

Conflicts of interest

There are no conflicts to declare.

Data availability

All data supporting this study are available within the article and its supplementary information (SI). Supplementary information: additional figures with catalyst characterization. See DOI: https://doi.org/10.1039/d6ra01056c.

Acknowledgements

This work was supported by JSPS KAKENHI (Grant Number 23K11479). The authors are grateful to Dr Koichi Igarashi for providing the K-M reactor, Prof. Koichi Tsuji for access to the XRF instrument and assistance during its use, and Prof. Yusuke Yamada for access to the XRD and Raman instruments. We also thank Haruto Fujiike for his assistance with Raman analyses, Prof. Masazumi Tamura for providing access to the H_2-TPR apparatus, Taichi Akiyama for his support in H_2-TPR measurements, Masatsugu Ishimoto for his assistance with TEM-EDS analyses, and Hiroki Sahara for his support in phenol decomposition experiments.

Notes and references

1 H. Matsuo, M. Kobayashi, S. Naniwa, *et al.*, *J. Phys. Chem. C*, 2023, **127**(19), 8946–8952.
2 S. Li, S. Zhao, S. F. Hung, *et al.*, *J. Am. Chem. Soc.*, 2025, **147**, 33770–33779.
3 Y. Ren, C. Song, H. Wang, *et al.*, *ACS Catal.*, 2024, **14**(6), 4340–4351.
4 C. Wang, X. K. Gu, H. Yan, *et al.*, *ACS Catal.*, 2017, **7**(1), 887–891.
5 B. Chen, B. Wu, L. Yu, *et al.*, *ACS Catal.*, 2020, **10**(11), 6176–6187.
6 H. Hosono, H. Saito, T. Higo, *et al.*, *J. Phys. Chem. C*, 2021, **125**(21), 11411–11418.
7 J. Sánchez, M. López-Haro, J. Hernández-Garrido, *et al.*, *J. Mater. Chem. A*, 2019, **7**(15), 8993–9003.
8 K. Yu, L. L. Lou, S. Liu, *et al.*, *Adv. Sci.*, 2020, **7**(2), 1901970.
9 X. Li, X. Wang, J. Ding, *et al.*, *ACS Catal.*, 2023, **13**(9), 6338–6350.
10 C. Hori, K. Ng, A. Brenner, *et al.*, *Braz. J. Chem. Eng.*, 2001, **18**, 23–33.
11 P. Janoš, T. Hladík, M. Kormunda, *et al.*, *Adv. Mater. Sci. Eng.*, 2014, **2014**(1), 706041.
12 S. Jiang, Z. You, N. Tang, *et al.*, *Processes*, 2023, **11**(7), 2087.

13 T. Cai, Z. Liu, J. Yuan, *et al.*, *Appl. Surf. Sci.*, 2021, **565**, 150596.

14 V. LaMer, R. Dinegar, *et al.*, *J. Am. Chem. Soc.*, 1950, **72**(11), 4847–4854.

15 N. Thanh, N. Maclean, S. Mahiddine, *et al.*, *Chem. Rev.*, 2014, **114**(15), 7610–7630.

16 M. Watzky, R. Finke, *et al.*, *Chem. Mater.*, 1997, **9**(12), 3083–3095.

17 S. Barkam, J. Ortiz, S. Saraf, *et al.*, *J. Phys. Chem. C*, 2017, **121**(36), 20039–20050.

18 K. Kai, Y. Yoshida, H. Kageyama, *et al.*, *J. Am. Chem. Soc.*, 2008, **130**(47), 15938–15943.

19 Z. Jia, D. Xiao, W. Yang, *et al.*, *J. Membr. Sci.*, 2004, **241**(2), 387–392.

20 H. Yao, Y. Wang, G. Luo, *et al.*, *Ind. Eng. Chem. Res.*, 2017, **56**(17), 4993–4999.

21 C. Han, A. Yoko, A. Taufik, *et al.*, *Chem. Mater.*, 2025, **37**(3), 1205–1214.

22 L. Gutierrez, L. Gomez, S. Irusta, *et al.*, *Chem. Eng. J.*, 2011, **171**(2), 674–683.

23 X. Huang, S. Xia, S. Lee, *et al.*, *ACS Appl. Nano Mater.*, 2023, **6**(10), 8574–8583.

24 S. Danjo, H. Yoshida, S. Hiraide, *et al.*, *Chem. Mater.*, 2025, **37**, 4778–4788.

25 S. Watanabe, T. Koshiyama, T. Watanabe, *et al.*, *Front. Chem. Eng.*, 2021, **3**, 780384.

26 Q. Xue, B. Yan, Y. Wang, *et al.*, *Chem. Eng. Sci.*, 2024, **278**, 118942.

27 Q. Xue, Z. Li, M. Chen, *et al.*, *Fuel*, 2021, **297**, 120785.

28 H. Nagasawa, N. Aoki, K. Mae, *et al.*, *Chem. Eng. Technol.*, 2005, **28**(3), 324–330.

29 S. Watanabe, S. Ohsaki, A. Fukuta, *et al.*, *Adv. Powder Technol.*, 2017, **28**(11), 3104–3110.

30 S. Asano, T. Maki, S. Inoue, *et al.*, Incorporative mixing in microreactors, *Chem. Eng. J.*, 2023, **451**, 138942.

31 H. Chen, A. Sayari, A. Adnot, *et al.*, *Appl. Catal., B*, 2001, **32**(3), 195–204.

32 L. Geng, B. Chen, J. Yang, *et al.*, *Appl. Catal., A*, 2020, **604**, 117774.

33 W. Yang, Y. Zhu, F. You, *et al.*, *Appl. Catal., B*, 2018, **233**, 184–193.

34 C. Ma, Y. Wen, C. Rong, *et al.*, *Catal. Sci. Technol.*, 2017, **7**(15), 3200–3204.

35 W. Yang, Z. Su, Z. Xu, *et al.*, *Appl. Catal., B*, 2020, **260**, 118150.

36 A. Stone, *et al.*, *Environ. Sci. Technol.*, 1987, **21**(10), 979–988.

37 F. Arena, G. Trunfio, J. Negro, *et al.*, *Mater. Res. Bull.*, 2008, **43**(3), 539–545.

38 K. Sing, D. Everett, R. Haul, *et al.*, *Pure Appl. Chem.*, 1985, **57**(4), 603–619.

39 C. Ma, Y. Wen, Q. Yue, *et al.*, *RSC Adv.*, 2017, **7**(43), 27079–27088.

40 V. Galakhov, M. Demeter, S. Bartkowski, *et al.*, *Phys. Rev. B: Condens. Matter Mater. Phys.*, 2002, **65**(11), 113102.

41 F. Larachi, J. Pierre, A. Adnot, *et al.*, *Appl. Surf. Sci.*, 2002, **195**(1–4), 236–250.

42 C. Julien, M. Massot, R. Baddour-Hadjean, *et al.*, *Solid State Ionics*, 2003, **159**(3–4), 345–356.

43 J. Post, D. McKeown, P. Heaney, *et al.*, *Am. Mineral.*, 2021, **106**(3), 351–366.

44 L. Gever, L. Enakonda, A. Pasi, *et al.*, *Nat. Commun.*, 2022, **13**(1), 2960.

45 K. Tonge, *et al.*, *Acta*, 1984, **74**(1–3), 151–166.

46 J. Chen, X. Chen, D. Yan, *et al.*, *Appl. Catal., B*, 2019, **250**, 396–407.